J Mol Model (2013) 19:109–118
DOI 10.1007/s00894-012-1519-8

ORIGINAL PAPER

Characterization of the structures and dynamics of phosphoric acid doped benzimidazole mixtures: a molecular dynamics study

Minal More · Swagata Pahari · Sudip Roy · Arun Venkatnathan

Received: 22 March 2012 / Accepted: 25 June 2012 / Published online: 22 July 2012
© Springer-Verlag 2012

Abstract Benzimidazole-based polymer membranes like poly(2,5-benzimidazole) (ABPBI) doped with phosphoric acid (PA) are electrolytes that exhibit high proton conductivity in fuel cells at elevated temperatures. The benzimidazole (BI) moiety is an important constituent of these membranes, so the present work was performed in order to achieve a molecular understanding of the BI–PA interactions in the presence of varying levels of the PA dopant, using classical molecular dynamics (MD) simulations. The various hydrogen-bonding interactions, as characterized based on structural properties and hydrogen-bond lifetime calculations, show that both BI and PA molecules exhibit dual proton-acceptor/donor functionality. An examination of diffusion coefficients showed that the diffusion of BI decreases with increasing PA uptake, whereas the diffusion of PA slightly increases. The hydrogen-bond lifetime calculations pointed to the existence of competitive hydrogen bonding between various sites in BI and PA.

Keywords Molecular dynamics · Radial distribution functions · Diffusion coefficient · Hydrogen bond

Electronic supplementary material The online version of this article (doi:10.1007/s00894-012-1519-8) contains supplementary material, which is available to authorized users.

M. More · A. Venkatnathan (✉)
Department of Chemistry,
Indian Institute of Science Education and Research,
Dr. Homi Bhabha Road,
Pune 411021, India
e-mail: arun@iiserpune.ac.in

S. Pahari · S. Roy (✉)
Physical Chemistry Division, National Chemical Laboratory,
Pune 411008, India
e-mail: s.roy@ncl.res.in

Introduction

Polymer electrolyte membrane (PEM) fuel cells are attractive choices for many technological applications, as they combine high energy efficiency with very low emissions of CO and CO_2. The polymer membrane is a critical component of the PEM fuel cell—it is responsible for proton conduction between the electrodes. Benzimidazole-based membranes like polybenzimidazole [1] (PBI) and poly(2,5-benzimidazole) (ABPBI) [2] have been investigated as fuel cell electrolytes. These membranes, when doped [3] with phosphoric acid (PA), have been used to operate PEM fuel cells at elevated temperatures [4, 5]. While PBI membranes have been extensively studied, ABPBI membranes have recently also started to receive significant attention. Chemically, a monomer unit of the ABPBI membrane consists of a single imidazole ring with two nitrogen atoms that serves as a proton acceptor [6] and can interact with an acid like PA. Due to the absence of the phenylene ring in ABPBI, it exhibits higher affinity towards PA than PBI does. PA-doped ABPBI membranes were shown [7] to display better conductivity and higher thermal stability than the corresponding PA-doped PBI membrane. Using FT-IR measurements, Asensio et al. [8] concluded that the nitrogen (N–H) of ABPBI serves as a proton donor. The authors observed the formation of $H_2PO_4^-$ anions, suggesting that proton transfer occurs via a Grotthuss [9] mechanism. Subsequently, Asensio et al. [10] also showed that PA-doped ABPBI membranes exhibit high proton conductivity, similar to PA-doped PBI membranes. Krishnan et al. [11] reported a conductivity of 2.6×10^2 S cm^{-1} at 180 °C when 1.2 molecules of PA were doped per monomer unit of ABPBI. The authors concluded that the poisoning of CO was limited, even beyond 170 °C. Wannek et al. [12] also demonstrated that PA-doped ABPBI membranes work efficiently during prolonged fuel cell operation.

While some experimental work [2] has been performed on PA-doped ABPBI membranes, the only published theoretical study on this topic is the work of Li et al. [13]. Those authors used classical molecular dynamics (MD) simulations to show that ABPBI has a higher affinity for PA than PBI does. Further, the authors concluded that the protonated oxygen atom of PA acts as a strong hydrogen acceptor. However, a detailed molecular level understanding of how benzimidazole interacts with PA has never been achieved. To attain this understanding, we investigated and characterized the various interactions of a benzimidazole (BI) molecule (a monomer unit of the ABPBI polymer membrane) with PA. Since we chose a BI molecule, parameters such as the chain length and orientation of the polymer membrane were obviously excluded from the study. We employed classical MD simulations to characterize the structural and dynamic properties of PA-doped BI mixtures at various temperatures. Further, we performed hydrogen-bond calculations on PA-doped BI mixtures. The results we obtained from this study, which are reported in the present paper, are important as they lead to a better understanding of the participation of the amine hydrogen of BI in hydrogen bonding with PA, and of the hydrogen-bonding interactions that occur between BI and PA molecules at various PA-dopant levels. The rest of the paper is organized as follows. The details of MD simulations are described in the following section. The results of our MD simulations are then discussed, before we finish by summarizing the salient results of our study.

Computational details

All MD simulations were performed using the GROMACS [14] 4.0.7 program. The chemical structures of the BI and PA molecules are shown in Fig. 1. The force-field parameters for BI were taken from the OPLS-AA force-field database [15], whereas the force-field parameters for PA were extracted from the work of Spieser et al. [16]. Two configurations containing 1,000 molecules of neat BI and neat PA were initially constructed. The resulting configurations were energy minimized using the steepest descent algorithm [17]. The minimized energy configurations of neat BI and neat PA were chosen as input for a subsequent equilibration. Various PA-doped BI mixtures were created by doping with different amounts of PA. In order to describe the compositions of these mixtures, we defined a parameter λ, which denotes the number of PA molecules for each BI molecule present in the mixture.

To check the effect of the initial configuration on the structural and dynamic properties of the mixtures, PA-doped BI mixtures were created using grid and solvated methods. The construction of input configurations using grid and solvated methods is now described using λ=2 as an example. The grid method (denoted by the letter "g" in tables and figures) consisted of arranging one BI molecule and two PA molecules regularly in a cubic box, and the process was repeated until a configuration containing 64 BI molecules and 128 PA molecules was obtained (see Fig. 2a). The solvated method (denoted by the letter "s" in tables and figures) was implemented by creating a configuration containing 64 BI molecules and subsequently solvating with 128 PA molecules, as seen in Fig. 2b. Using the grid and solvated methods, input configurations with λ=4, 8, and 12 were also generated. In order to sample the conformational space, the energy-minimized configuration for each λ was chosen as input for the simulated annealing procedure. Using a timestep of 2 fs and the NPT ensemble, a simulated annealing method for each λ was performed, as follows. Each configuration was heated from 450 K to 660 K and cooled back to 450 K in steps of 30 K, with a total simulation time of 5.2 ns per cycle. The annealing procedure was repeated five times, and the final configuration was chosen as input for a subsequent equilibration.

For all of the MD simulations, the cut-off for van der Waals and electrostatic interactions was chosen as 1.0 nm. The timestep was 1 fs and the leapfrog algorithm [18] was used as an integrator for the equation of motion. Each MD simulation was equilibrated for 10 ns using the NPT ensemble with an isotropic pressure of 1 bar and a Berendsen barostat [19]. Temperature was kept constant using a velocity-rescale thermostat [20] with a coupling time of 0.1 ps. The particle mesh Ewald [21, 22] (PME) method was used to calculate long-range electrostatic interactions. Equilibration was followed by a 20 ns production run using the NPT ensemble with the Nosé–Hoover thermostat [23, 24] and the Parrinello–Rahman barostat [25, 26]. MD equilibration and production runs with neat BI and neat PA were performed from 325 K to 475 K, and with PA-doped BI mixtures at 350 K, 400 K, and 450 K. Trajectories from the production runs were recorded every 5 ps to calculate the density, radial distribution functions, mean square displacement, and the diffusion of each neat system and PA-doped BI mixture.

Results and discussion

Densities, structures, and dynamics of the neat systems

Before we investigated the structural and dynamic properties of PA-doped BI mixtures, we calculated the properties of neat BI and neat PA and checked them against existing experimental/theoretical data for validation purposes. The computed average densities for the neat BI and neat PA as a function of temperature are shown in Fig. 3. The simulated density (1.14 $g cm^{-3}$) of neat BI at 325 K is in reasonable

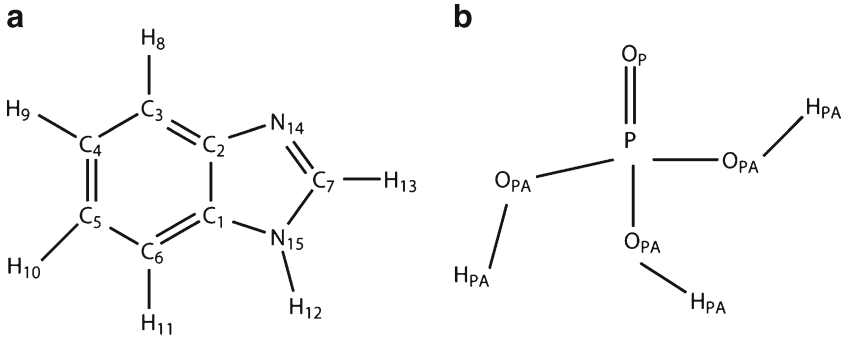

Fig. 1 **a**–**b** Chemical structures of **a** BI and **b** PA. (The atom types for these structures are used in RDFs and HB)

agreement with the experimental density [27] (1.22 gcm^{-3}) of BI at 298 K. Similarly, the simulated density (1.84 gcm^{-3}) of PA at 325 K is in reasonable agreement with a previously calculated density [16] (1.89 gcm^{-3}) at 300 K, and is in excellent agreement with the experimental density [28] (1.845 gcm^{-3}) at 333 K. Our calculated densities of neat BI and neat PA barely change over a wide temperature range (T= 325–475 K). The radial distribution functions (RDFs) of the neat BI and neat PA are shown in Fig. 4. The qualitative features of the RDFs are very similar at all temperatures. The RDFs can be classified based on interactions: intermolecular hydrogen bonding between atoms in neat BI and neat PA, and center-of-mass interactions between BI molecules and between PA molecules. For example, the N_{14}–H_{12} RDFs (atom numbers are shown in Fig. 1) show the presence of intermolecular hydrogen bonding in neat BI. The hydrogen-bond lengths are evident from a first peak at 1.6 Å and a minimum at 2.4 Å. An examination of the BI_{com}–BI_{com} RDFs ("com" denotes the center of mass) shows a first minima at 8 Å with a coordination number of 12.5. This large coordination number shows the theoretical maximum number of BI molecules that can exist in the first solvation shell, and also provides a benchmark for comparing BI–BI interactions in PA-doped BI mixtures. The H_{PA}–O_P RDFs in neat PA show strong intermolecular hydrogen bonding between the nonprotonated oxygen (O_P) and hydrogen (H_{PA}). The H_{PA}–O_P RDFs show a first peak at 2 Å, a minimum at 2.8 Å, and are consistent with experimental data [29]. The PA_{com}–PA_{com} RDFs show a first peak at 4.8 Å and agree well with the results reported by Tsuchida [30]. The PA_{com}–PA_{com} RDFs show a first minimum at 6.5 Å, corresponding to a coordination number of 13.13. This large solvation shell of PA reflects the high density of the system.

The mobilities of neat BI and neat PA are gauged from the mean square displacement (MSD), which is calculated using the Einstein equation [18], written as

$$\lim_{t\to\infty}\left\langle \|r_i(t)-r_i(0)\|^2\right\rangle_{i\in A}=6D_At, \quad (1)$$

where r_i is the center-of-mass position of any molecule and D_A is the corresponding self-diffusion coefficient (of either BI or PA), calculated from the linear regime of the corresponding MSD (see Fig. S1). As seen from Table 1, the diffusion coefficients of neat BI and neat PA increase with temperature. The increase in the diffusion coefficient is larger for PA than for BI. The diffusion coefficients calculated in this work for different temperatures were compared with the diffusion in PA-doped BI mixtures. The diffusion of neat PA calculated in this work (0.06×10^{-7} cm^2 s^{-1} at 325 K) is in excellent agreement with the simulated diffusion coefficient (0.1×10^{-7} cm^2 s^{-1} at 300 K) reported by Spieser et al. [16]. The diffusion of neat PA observed in experimental measurements [31] is 1.75×10^{-7} cm^2 s^{-1} (315 K), and is an order of magnitude larger than the simulated diffusion coefficients. The higher value of the

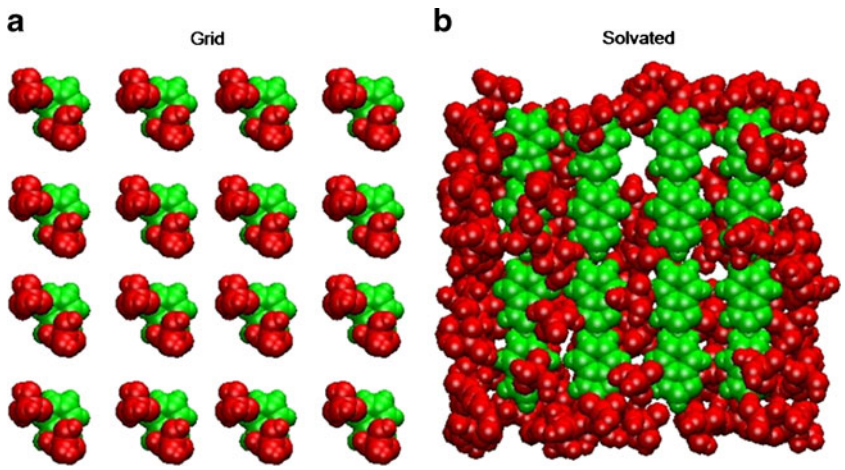

Fig. 2 **a**–**b** Initial configuration of λ=2 (*green* BI, *red* PA) using **a** grid and **b** solvated methods

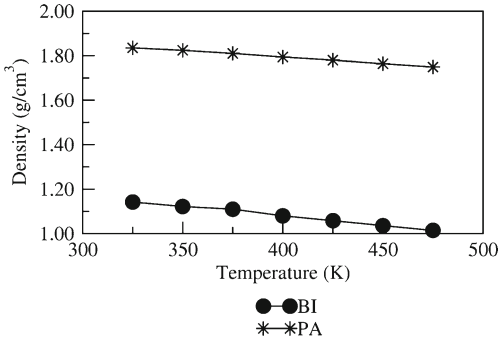

Fig. 3 Densities of neat BI and neat PA

Table 1 Diffusion coefficients ($\times 10^{-7}$ cm^2 s^{-1}) obtained for neat BI and neat PA

T (K)	BI	PA
325	4.95	0.06
350	16.10	0.26
375	33.85	0.68
400	57.51	1.81
425	93.22	3.55
450	137.80	6.39
475	198.10	10.70

experimental diffusion coefficient is due to the presence of phosphate anions in neat PA. The activation energy for the diffusion of neat PA according to our simulations is 44 kJ mol^{-1}, and is higher than the calculated activation energy of 24 kJ mol^{-1} reported by Li et al. [32]. The difference in activation energy between our simulations and the work of Li et al. [32] is due to the choice of force field used in the simulations. This can be seen in the simulated density of Li et al. [32], which shows a deviation of ~12 % from the experimental density of PA.

Effect of input configuration on the structures and dynamics of PA-doped BI mixtures

The computed densities of the PA-doped BI mixtures (from the grid and solvated configurations) at various temperatures based on 10 ns of MD equilibration is shown in Table 2. For the grid and solvated configurations, the densities of the PA-doped BI mixtures decrease linearly with temperature. The differences between the densities (for all λ and T) obtained using the grid configuration and those obtained with the solvated configuration are very insignificant. The structural rearrangements that occur in PA-doped BI mixtures for the grid and solvated configurations can be seen by examining the RDFs between the nitrogen (N_{14} and N_{15}) atoms and the phosphorus (P) atom (shown in Fig. 5a, b). The RDFs calculated (for all λ and T) using the grid and solvated configurations show very similar features. The diffusion coefficients calculated (for all λ and T) from the grid and solvated configurations (see Fig. 5c, d) are also similar. Hence, a comprehensive examination of the densities, RDFs, and diffusion coefficients obtained using the grid and solvated configurations of PA-doped BI mixtures

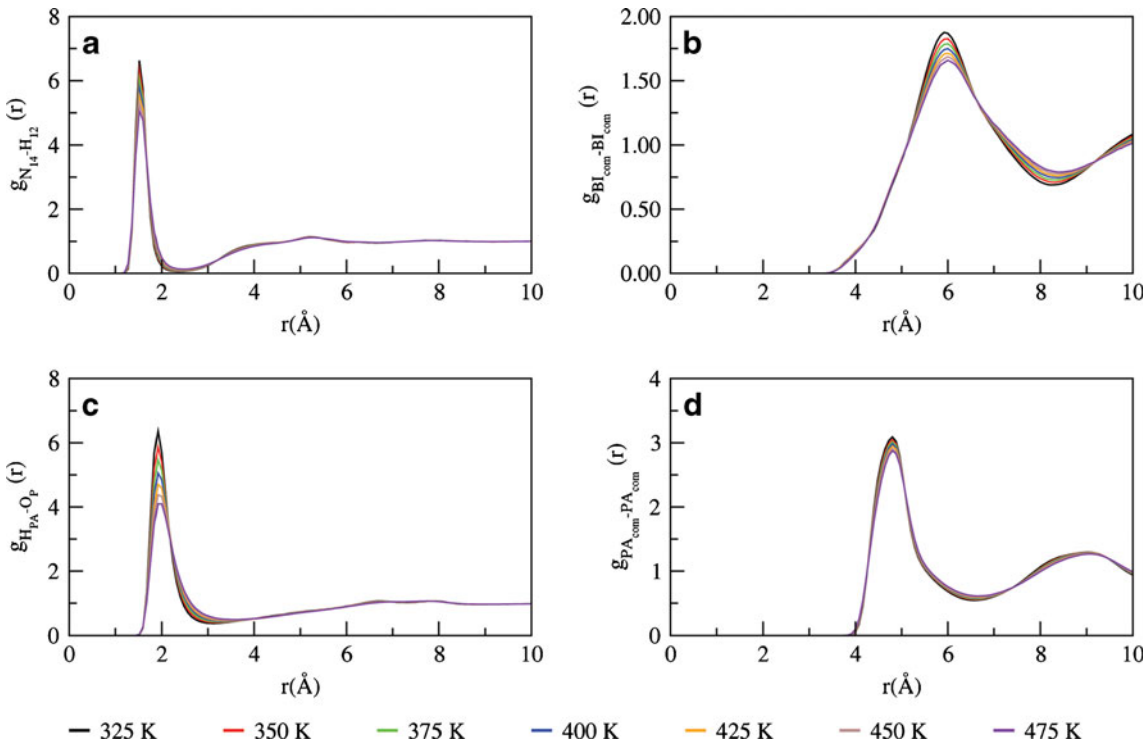

Fig. 4 **a**–**d** RDFs of **a** N_{14}–H_{12}, **b** BI_{com}–BI_{com}, **c** H_{PA}–O_P, and **d** PA_{com}–PA_{com}

Table 2 Densities (g cm^{-3}) obtained for PA-doped BI mixtures from the grid (g) and solvated (s) configurations

T (K)	λ=2		λ=4		λ=8		λ=12	
	g	s	g	s	g	s	g	s
350	1.485	1.483	1.601	1.605	1.696	1.689	1.732	1.734
400	1.454	1.453	1.574	1.573	1.662	1.663	1.703	1.703
450	1.423	1.424	1.541	1.541	1.632	1.633	1.671	1.672

indicated that the choice of input configuration does not influence any properties. To eliminate any finite-size effect, the configuration corresponding to each λ (obtained from the production run) was replicated twice in each direction of the cubic box. Since we found that simulations using grid and solvated input configurations showed similar properties, we chose to use only the solvated configuration to create the replicated PA-doped BI mixtures. The replicated mixture (for each λ) was equilibrated for a further 10 ns. The densities of the replicated mixtures (calculated based on the equilibration runs) are shown in Table S1 of the "Electronic supplementary material." Further, all RDFs, MSDs, and diffusion coefficients shown in subsequent sections were calculated based on the 20 ns production runs for the replicated mixtures.

Influence of PA uptake on the intermolecular interactions in PA-doped BI mixtures

The intermolecular interaction between the imine nitrogen (N_{14}) and the amine hydrogen (H_{12}) in BI (in the PA-doped BI mixtures) can be explored using the N_{14}–H_{12} RDFs shown in Fig. 6a. The imine nitrogen, which contains a lone pair of electrons, acts as a hydrogen acceptor (via hydrogen bonding) from the amine hydrogen. The first minimum in these RDFs appears at 2.9 Å (for all λ) and corresponds to a coordination number (see Table 3) of 0.3 (λ=2) or 0.05 (λ=12).This decrease in coordination number shows that the tendency for the imine nitrogen (N_{14}) and amine hydrogen atoms to form a hydrogen bond decreases with increasing λ.

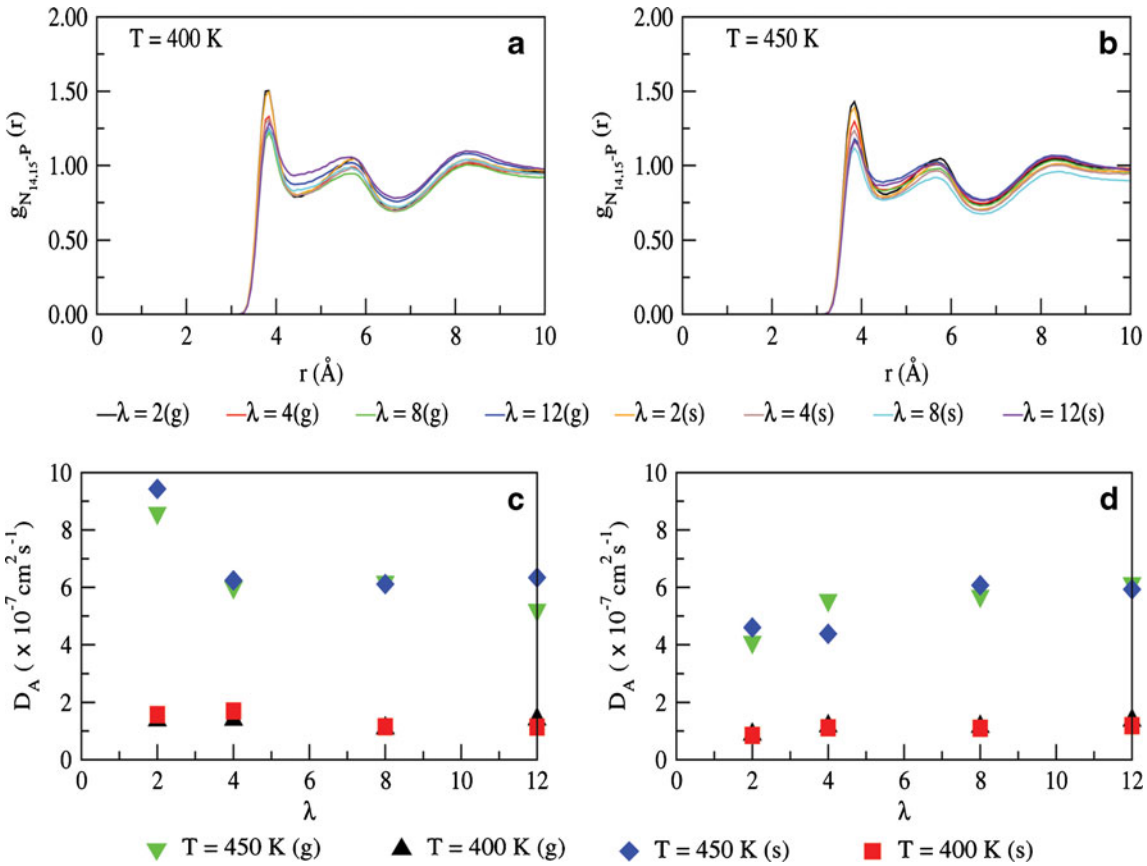

Fig. 5 **a**–**d** $N_{14,15}$-P RDFs obtained from the grid and solvated configurations at **a** 400 K and **b** 450 K. Diffusion coefficients of **c** BI and **d** PA at 400 K and 450 K are also shown

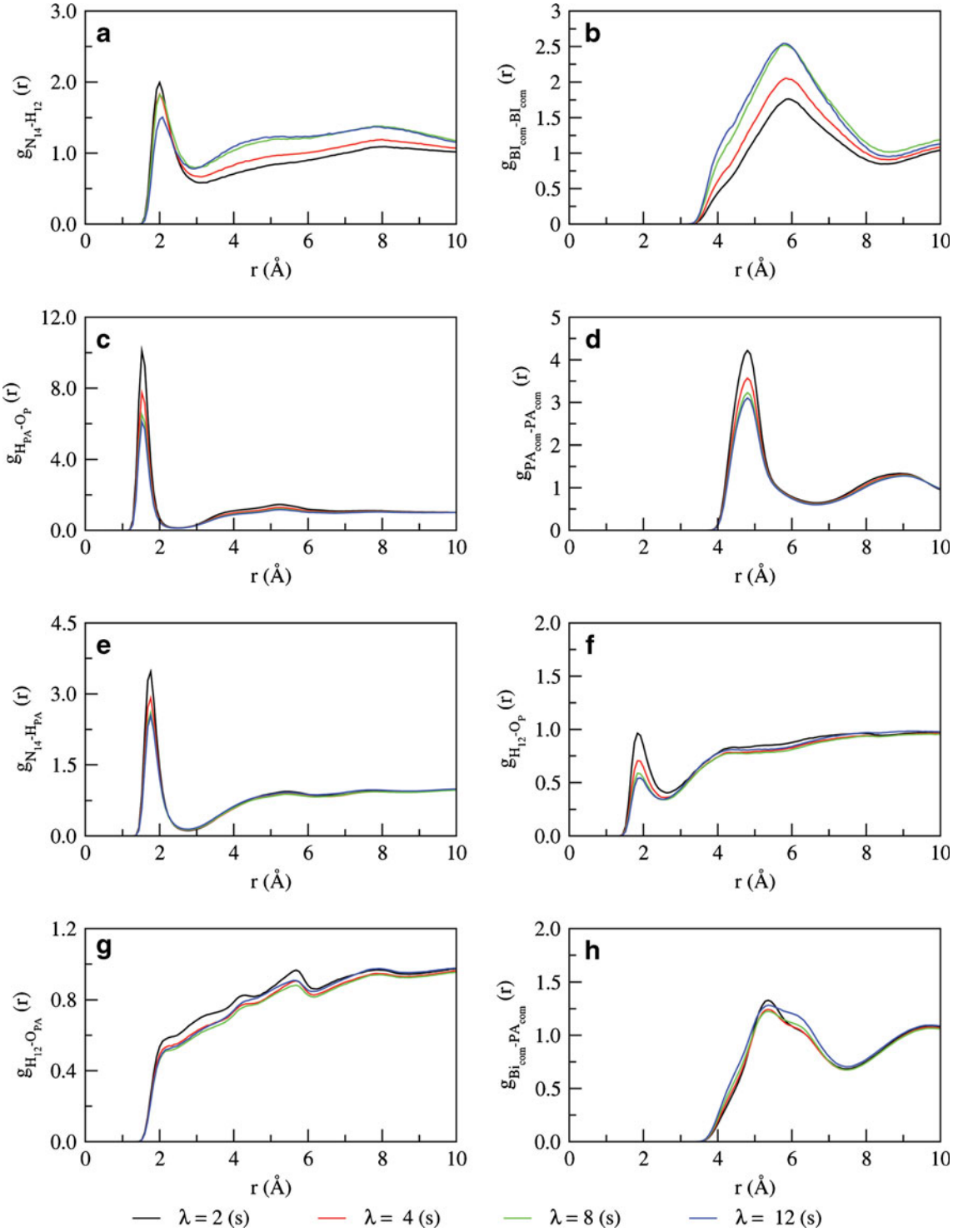

Fig. 6 **a**–**h** RDFs of PA-doped BI mixtures at 450 K for **a** N_{14}–H_{12}, **b** BI_{com}–BI_{com}, **c** H_{PA}–O_P, **d** PA_{com}–PA_{com}, **e** N_{14}–H_{PA}, **f** H_{12}–O_P, **g** H_{12}–O_{PA}, and **h** BI_{com}–PA_{com}

Due to the presence of a large number of PA molecules, there is significant separation between any two BI molecules, which shows that the peak height for the length of the hydrogen bond between the N_{14} and H_{12} atoms decreases with λ. The BI_{com}–BI_{com} RDFs presented in Fig. 6b show a minimum at 8.5 Å, corresponding to a coordination number

Table 3 Coordination numbers calculated at the first minimum at 450 K

λ	N_{14}–H_{12}	BI_{com}–BI_{com}	H_{PA}–O_P	PA_{com}–PA_{com}	N_{14}–H_{PA}	H_{12}–O_P	H_{12}–O_{PA}	BI_{com}–PA_{com}
2	0.30	7.75	0.60	8.15	1.05	0.64	0.34	3.50
4	0.19	5.90	0.70	10.20	1.30	0.25	0.36	9.75
8	0.10	4.40	0.71	11.20	1.42	0.20	0.38	12.50
12	0.05	2.80	0.75	12.50	1.50	0.19	0.50	13.75
Neat BI	1.10	12.50	–	–	–	–	–	–
Neat PA	–	–	0.79	13.13	–	–	–	–

of 7.75 (λ=2) or 2.80 (λ=12). This decrease in coordination number with λ is due to the increasing solvation of the BI molecules by PA. The intermolecular H_{PA}–O_P RDFs in Fig. 6c show a very sharp peak at 1.5 Å, where there is strong hydrogen bonding, and such observations are consistent with the experimental data of Tromp et al. [29] and the previous results for neat PA reported by Tsuchida [30]. The H_{PA}–O_P RDFs show a first minimum at 2.50 Å corresponding to a coordination number of 0.60 (λ=2) or 0.75 (λ=12). The slight increase in coordination number shows that there is marginal increase in intermolecular hydrogen bonding with increasing λ. The PA_{com}–PA_{com} RDFs in Fig. 6d show a first peak at 4.95 Å and a minimum at 6.5 Å, consistent with the results reported by Tsuchida [30] for neat PA. The coordination number obtained at this minimum in the PA_{com}–PA_{com} RDFs increases from 8.15 (λ=2) to 12.50 (λ=12), which shows that increasing λ results in large solvation shells that are rich in PA molecules. The N_{14}–H_{PA} RDFs in Fig. 6e show a first minimum at 2.5 Å. The first peak position in the N_{14}–H_{PA} RDFs appears at 1.75 Å. The coordination number at the first minimum increases from 1.05 (λ=2) to 1.5 (λ=12). The increase in coordination number with λ occurs because the H_{PA} hydrogen is acidic in nature and prefers to orient around the imine nitrogen (N_{14}). An interaction between the amine hydrogen (H_{12}) of BI and the double-bonded nonprotonated oxygen (O_P) of PA can be discerned by examining the H_{12}–O_P RDFs shown in Fig. 6f. The decrease in coordination number (obtained at the first minimum at 2.5 Å) with increasing λ demonstrates the poor ability of the amine hydrogen to participate in hydrogen bonding with the nonprotonated oxygen (O_P) of PA. The RDFs between the amine hydrogen (H_{12}) and the protonated oxygen (O_{PA}) are shown in Fig. 6g. Unlike the other RDFs, the H_{12}–O_{PA} RDFs do not show a sharp minimum. However, we can see a small shoulder at 2.2 Å, which was chosen as the cutoff when calculating the coordination number at each λ. The coordination number increases from 0.34 (λ=2) to 0.50 (λ=12). An examination of the coordination numbers obtained from the H_{12}–O_{PA} and H_{12}–O_P RDFs in Table 3, shows that the strength of the interaction of the amine hydrogen (H_{12}) with the protonated oxygen atom (O_{PA}) increases with increasing λ, whereas there is a decrease in the interaction strength with the nonprotonated oxygen (O_P). The coordination numbers also offer indirect evidence that at large values of λ, the Grotthuss mechanism for proton transfer in PA-doped BI mixtures is more likely to occur via hydrogen bonding between the protonated oxygen (O_{PA}) of PA and the amine hydrogen (H_{12}) of BI (although this needs to be confirmed by ab initio MD simulations). The solvation of BI by PA molecules can be seen in the BI_{com}–PA_{com} RDFs shown in Fig 6h. Similar to the trends seen for the PA_{com}–PA_{com} RDFs, the coordination number increases from 3.50 (λ=2) to 13.75 (λ=12).

Influence of the PA uptake and temperature on diffusion

The diffusion coefficients calculated from the MSDs (see Fig. S2 of the "Electronic supplementary material") are

Table 4 Diffusion coefficients ($\times 10^{-7}$ cm^2 s^{-1}) obtained for BI and PA in replicated PA-doped BI mixtures based on the solvated configuration

λ	*T* (K)	BI	PA
2	350	0.20±0.04	0.09±0.01
	400	1.74±0.18	1.00±0.01
	450	9.29±0.67	5.37±0.13
4	350	0.11±0.01	0.08±0.00
	400	1.18±0.18	0.96±0.01
	450	7.40±0.51	5.74±0.03
8	350	0.13±0.03	0.11±0.00
	400	1.27±0.01	1.35±0.01
	450	6.21±0.27	6.10±0.33
12	350	0.16±0.04	0.14±0.01
	400	1.27±0.08	1.42±0.01
	450	5.87±0.23	6.10±0.02

shown in Table 4. For example, the diffusion of BI in PA-doped BI mixtures at 450 K was slower by a factor ranging from 14.83 (λ=2) to 23.47 (λ=12) compared to the diffusion of neat BI. However, the diffusion of PA in PA-doped BI mixtures at 450 K differed from that of neat PA by much smaller factors: 1.18 (λ=2) to 1.04 (λ=12). This shows that the diffusion of BI in PA-doped BI mixtures is significantly slower than the diffusion of neat BI, because the BI molecules can be trapped in the strong hydrogen-bonded network formed by the PA molecules. This observation is consistent with the RDFs (Fig. 6e), which show that there is significant hydrogen bonding between the hydrogen (H_{PA}) of PA and the imine nitrogen (N_{14}) of BI. Further, the vehicular diffusion of PA barely changes as the amount of PA increases. Similar trends in the diffusion coefficients of BI and PA in PA-doped BI mixtures with various PA-doping levels were also observed at 350 K and 400 K. The effects of temperature on the diffusion are as follows. The diffusion of BI in PA-doped BI mixtures increases by a factor of~9 (λ=2) from 350 K to 450 K. Similarly, the diffusion of PA in PA-doped BI mixtures increases by factor of~6 (λ=2) from 350 K to 450 K. Indeed, increases in the diffusion coefficient with temperature are seen for all λ. For each temperature, the diffusion of BI decreases as λ increases, whereas the diffusion of PA increases.

Influence of PA uptake on the hydrogen-bond dynamics

Characterizing the formation and scission of hydrogen bonds (HBs) is a useful way to gain an understanding of proton transport mechanisms. Since classical force fields do not allow bond breaking or formation, we focused our attention solely on the uninterrupted HB dynamics, which can be captured in the following manner. The HB dynamics are much faster than the self-diffusion of each type of molecule; hence, if a HB is broken, the same molecule could remain in the vicinity for some time before the same bond is reformed. Similar to the work of Spoel et al. [33], the HB analysis performed in this work was realized in the following manner. The final snapshots of the various PA-doped BI mixtures from a 20 ns production run at 450 K were chosen as input, and a short 250 ps production run was performed where the trajectories were recorded every 50 fs. The hydrogen bond probability distribution was calculated, where the length of the HB was considered to be the distance between the donor and acceptor atoms that participate in the hydrogen bonding [34–36] (see Fig. S3 of the "Electronic supplementary material"), while the HB angle was considered to be the angle donor–hydrogen–acceptor (see Fig. S4 of the "Electronic supplementary material"). The maximum cutoff distance and angle applied when calculating the HB dynamics (for each interaction and λ) were chosen based on Figs. S3 and S4, respectively. The HB lifetime was calculated using the autocorrelation function $C(t)$ [37, 38]:

$$C(t) = \frac{\langle h(0)|h(t)\rangle}{\langle h(0)|h(0)\rangle}, \quad (2)$$

where $h(t)$=1 if a pair is found to be linked by a hydrogen bond at time t, and 0 otherwise. The integral [33] of $C(t)$ gives an estimate for the average HB lifetime, τ_{HB}:

$$\tau_{HB} = \int_0^\infty C(t)dt. \quad (3)$$

For each interaction and λ, the HB number was normalized with respect to the number of PA molecules. Additionally, the HB number for the H_{12}–O_{PA} interaction was normalized with respect to the number of O_{PA} sites. The HB number and correlation times [$C(t)$] corresponding to the HB interactions are shown in Fig. 7. The HB number for N_{14}–H_{12} decreases, that for H_{PA}–O_P increases, that for N_{14}– H_{PA} decreases, that for H_{12}–O_P decreases, and that for H_{12}–O_{PA} decreases with λ. The HB lifetimes are shown in Table 5. The HB lifetimes for H_{PA}–O_P, N_{14}–H_{PA}, and H_{12}–O_P decrease with λ. The HB lifetime for the H_{12}–O_{PA} interaction increases with λ. However, we observed a corresponding decrease in the HB lifetime of H_{12}–O_P with λ, and this is due to the competition between the HBs N_{14}–H_{12} and H_{12}–O_{PA}. The increase in the HB lifetime of the H_{12}–O_{PA} bond with increasing λ, in contrast to the decrease in the HB lifetime of the H_{12}–O_P bond, illustrates the strength of the interaction of the amine hydrogen (H_{12}) with the protonated oxygen (O_{PA}) as opposed to that with the nonprotonated oxygen (O_P) of PA. Our MD simulations suggest that both BI and PA can act as proton acceptors and proton donors. However, such conclusions need to be confirmed by ab initio molecular dynamics (AIMD), which can show the actual process of proton transfer, including the formation and scission of hydrogen bonds.

Concluding remarks

The structural and dynamic properties of neat BI, neat PA, and PA-doped BI mixtures were characterized by MD simulations. Different choices for the input configurations of the PA-doped BI mixtures resulted in similar structural and dynamical properties. The RDFs showed that temperature has only a limited effect on the structural changes in the neat BI, neat PA, and PA-doped BI mixtures. The RDFs for the PA-doped BI mixtures show the presence of a strong hydrogen bond between the imine nitrogen (N_{14}) of BI and the hydrogen (H_{PA}) of PA where the imine nitrogen accepts the hydrogen from PA, which is further confirmed by HB analysis. The coordination numbers (Table 3) and HB lifetimes (Table 5) show that with increasing PA uptake, the

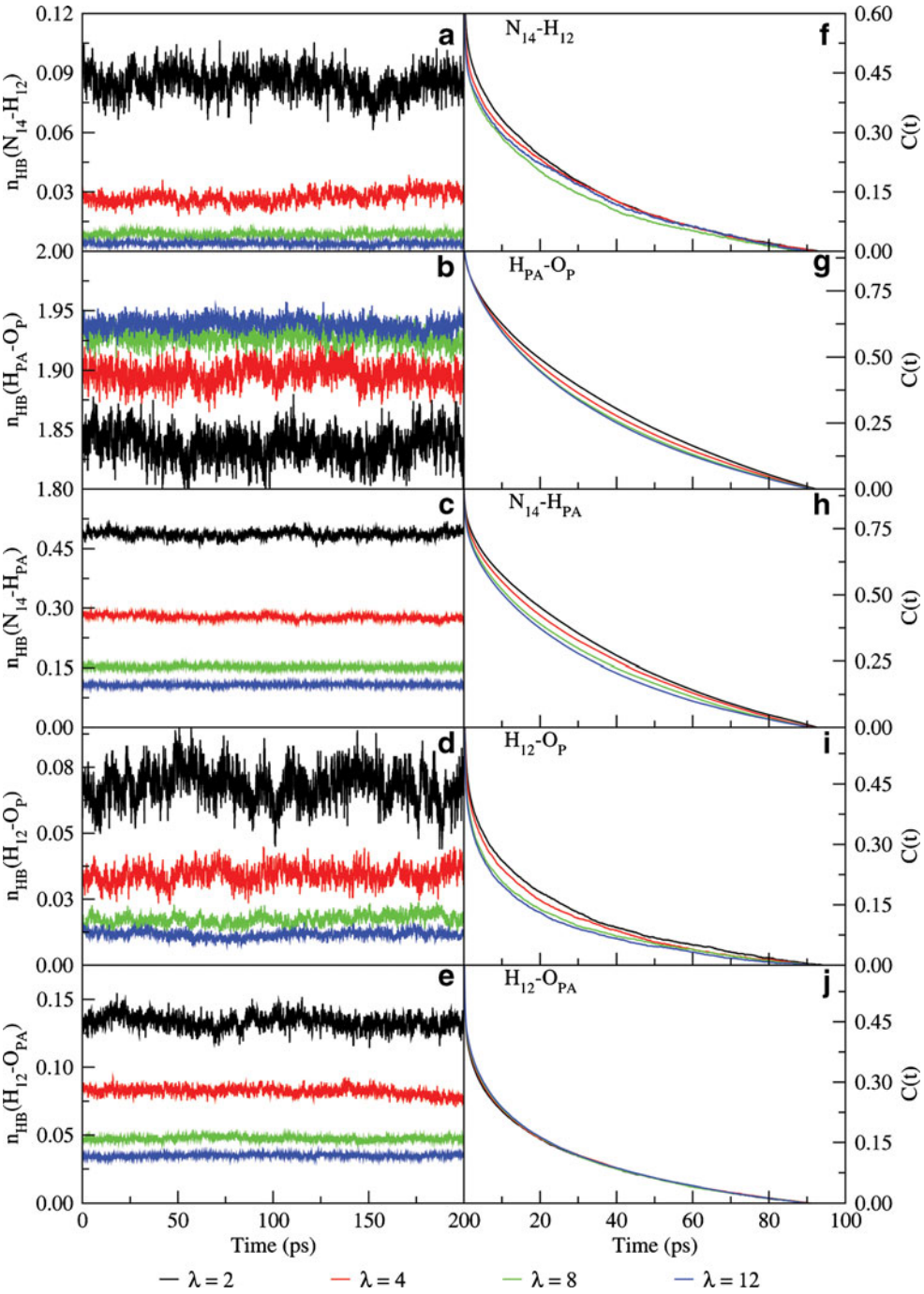

Fig. 7 **a–j** HB numbers **a–e** and lifetimes **f–j** of PA-doped BI mixtures at 450 K

Table 5 HB lifetimes (in ps) in a 250 ps production run

λ	N_{14}–H_{12}	H_{PA}–O_P	N_{14}–H_{PA}	H_{12}–O_P	H_{12}–O_{PA}
2	13.21	27.11	24.60	10.32	9.01
4	12.62	25.59	23.08	9.30	9.18
8	11.08	24.47	21.31	8.19	9.15
12	12.07	24.10	20.17	7.61	9.29

interaction between the amine hydrogen (H_{12}) of BI and the protonated oxygen (O_{PA}) of PA increases in strength, whereas the interaction between the amine hydrogen (H_{12}) of BI and the nonprotonated oxygen (O_P) of PA decreases. The diffusion of BI decreases with increasing PA uptake. However, the vehicular diffusion of PA shows a marginal increase with increasing PA uptake, so computational methods that consider structural diffusion must be used. The study of structural diffusion in PA is very likely to provide a clear understanding of proton transport in PA, and this will

be the focus of our future research. Nevertheless, the results presented in this work characterize the various hydrogen-bonding interactions between BI and PA. The molecular-level understanding of how BI interacts with PA enabled by this study can assist in the design and development of benzimidazole-based polymer electrolyte membranes.

Acknowledgments This work used the computing resources provided by the Indian Institute of Science Education and Research, Pune (IISER Pune), and the National Chemical Laboratory, Pune. MM acknowledges IISER Pune for graduate fellowship support. SP acknowledges the Council of Scientific and Industrial Research (CSIR) for fellowship support. The authors thank Anurag Prakash Sunda for useful discussions. AV acknowledges the Department of Science and Technology (SR/S1/PC/28/2009) and the Department of Science and Technology, Nanomission (SR/NM/NS-42/2009) for financial support. SR and AV acknowledge the CSIR XIth Energy Plan (NWP-0022-1) for financial support.

References

1. Musto P, Karasz FE, MacKnight W (1993) Polymer 34:2934–2945
2. Asensio JA, Sánchez EM, Gómez-Romero P (2010) Chem Soc Rev 39:3210–3239
3. Xing B, Savadogo O (1999) J New Mater Electrochem Syst 2:95–101
4. Dippel T, Kreuer KD, Lassègues JC, Rodriguez D (1993) Solid State Ionics 61:41–46
5. Schuster MFH, Meyer WH, Schuster M, Kreuer KD (2004) Chem Mater 16:329–337
6. Rodriguez D, Jegat C, Trinquet O, Grondin J, Lassègues JC (1993) Solid State Ionics 61:195–202
7. Litt MH, Ameri R, Wang Y, Savinell RF, Wainright JS (1999) Mater Res Soc Symp Proc 548:313–324
8. Asensio JA, Borrós S, Gómez-Romero P (2004) J Electrochem Soc 151:A304–A310
9. Agmon N (1995) Chem Phys Lett 244:456–462
10. Asensio JA, Gomez-Romero P (2005) Fuel Cells 5:336–343
11. Krishnan P, Park JS, Kim CS (2006) J Power Sources 159:817–823
12. Wannek C, Kohnen B, Oetjen HF, Lippert H, Mergel J (2008) Fuel Cells 8:87–95
13. Li S, Fried JR, Colebrook J, Burkhardt J (2010) Polymer 51:5640–5648
14. Hess B, Kutzner C, van der Spoel D, Lindahl E (2008) J Chem Theor Comput 4:435–447
15. Jorgensen WL, Tirado-Rives J (1988) J Am Chem Soc 110:1657–1666
16. Spieser SAH, Leeflang BR, Kroon-Batenburg LMJ, Kroon J (2000) J Phys Chem A 104:7333–7338
17. Payne MC, Teter MP, Allan DC, Arias TA, Joannopoulos JD (1992) Rev Mod Phys 64:1045–1097
18. Allen MP, Tildesley DJ (1987) Computer simulation of liquids. Oxford Science, New York
19. Berendsen HJC, Postma JPM, van Gunsteren WF, DiNola A, Haak JR (1984) J Chem Phys 81:3684–3690
20. Bussi G, Donadio D, Parrinello M (2007) J Chem Phys 126:014101–014107
21. Darden T, York D, Pedersen L (1993) J Chem Phys 98:10089–10092
22. Essmann U, Perera L, Berkowitz ML, Darden T, Lee H, Padersen LG (1995) J Chem Phys 103:8577–8593
23. Nosé S (1984) Mol Phys 52:255–268
24. Hoover WG (1985) Phys Rev A 31:1695–1697
25. Parrinello M, Rahman A (1981) J Appl Phys 52:7182–7190
26. Nosé S, Klein ML (1983) Mol Phys 50:1055–1076
27. Vijayan N, Balamurugan N, Ramesh Babu R, Gopalakrishnan R, Ramasamy P, Harrison WTA (2004) J Crystal Growth 267:218–222
28. Egan EP, Luff BB (1955) Ind Eng Chem 47:1280–1281
29. Tromp RH, Spieser SH, Neilson GW (1999) J Chem Phys 110:2145–2150
30. Tsuchida EJ (2006) J Phys Soc Jpn 75:54801–54805
31. Dippel T, Kreuer KD, Lassegues JC, Rodriguez D (1993) Solid State Ionics 61:41–46
32. Li S, Fried JR, Sauer J, Colebrook J, Dudis DS (2011) Int J Quantum Chem 111:3212–3229
33. Van der Spoel D, van Maaren PJ, Larsson P, Tîmneanu N (2006) J Phys Chem B 110:4393–4398
34. Luzar A, Chandler D (1993) J Chem Phys 98:8160–8173
35. Starr FW, Nielsen JK, Stanley HE (1999) Phys Rev Lett 82:2294–2297
36. Starr FW, Nielsen JK, Stanley HE (2000) Phys Rev E 62:579–587
37. Stillinger FH (1975) Adv Chem Phys 31:1–101
38. Luzar A, Chandler D (1996) Nature 379:55–57